Biomaterials Science

ROYAL SOCIETY OF CHEMISTRY

PAPER

View Article Online
View Journal

Check for updates

Cite this: DOI: 10.1039/d2bm01332k

Super-resolution traction force microscopy with enhanced tracer density enables capturing molecular scale traction†

Yue Xu,[a] Chuanwen Guo,[a] Xueyi Yang,[a] Weihong Yuan,[b] Xu Zhang,[a] Yujie Sun,[b] Gang Wen,[c] Linbo Wang,[c] Hui Li,*[c] Chunyang Xiong *[d] and Chun Yang*[a]

Received 20th August 2022,
Accepted 7th December 2022

DOI: 10.1039/d2bm01332k

rsc.li/biomaterials-science

Cell traction mediates the biochemical and mechanical interactions between the cell and its extracellular matrix (ECM). Traction force microscopy (TFM) is a powerful technique for quantitative cellular scale traction analysis. However, it is challenging to characterize macromolecular scale traction events with current TFM due to the limited sampling density and algorithmic precision. In this article, we introduce a super-resolution TFM by utilizing a novel substrate surface modification method. Our TFM technique achieved a spatial resolution comparable to fluorescence microscopy and precision comparable to the rupture force of an integrin–ligand bond. Correlated imaging of TFM with fluorescence microscopy demonstrated that the residing paxillin highly correlated with traction while α5 integrin was located differently. Time-lapse TFM imaging captured a transient traction variation as the adhesion protein passed by. Thus, the novel super-resolution TFM benefits the studies on cellular biochemical and mechanical interactions.

Published on 22 December 2022. Downloaded by Tsinghua University on 1/9/2023 2:11:16 PM.

Introduction

Cells and their extracellular environment undergo complicated crosstalk, sustaining tissue homeostasis, orchestrating tissue growth, or driving diseases once misbalanced.[1] The dynamic interplay between the cell and its extracellular matrix (ECM) includes biochemical signal transmission, such as cytokine-receptor binding, and mechanical interactions, such as cell traction.[2] Cell traction is initiated by actomyosin contractility in stress fibres and is transmitted to the ECM by actin–integrin–ligand linkage.[3] Cell traction has been proven to take part in various life activities, including cell migration,[4] cell differentiation,[5] and immune response.[6,7]

Molecular tension fluorescence microscopy[8–10] (MTFM) and traction force microscopy[11–18] (TFM) are two of the most widely used methods for evaluating cell traction. Although MTFM performs better than TFM in spatial resolution (50 nm)[19] and single-molecule force measurement,[20] MTFM requires cells to be placed on glass (whose mechanical properties are very different from the *in vivo* environment) and a total internal reflection fluorescence (TIRF) microscopy to guarantee high resolution and precision. For TFM tests, cells are cultured on a biocompatible substrate whose elasticity can be tuned to mimic biological tissues,[5] and almost all common fluorescence microscopies can be used.[4,21,22] TFM outputs an intact traction vector map, while MTFM cannot detect the force direction. Thus, TFM is more preferable for biological research as it is closer to the physiological conditions, easy operation, and a more detailed traction output.

In a TFM experiment, cells are plated on a linear elastic substrate, usually polyacrylamide (PAAM).[23] Fluorescent beads are embedded in the close vicinity or conjunct to the surface of the substrate as deformation tracers.[13,17,24] As the cells adhere to the substrate and exert force through their adherent patches, the subsequent substrate deformation can be tracked by measuring the displacement of the tracer beads. Given the displacement field and the elastic parameter of the substrate, the cellular traction field can be reconstructed by an inverse elastic half-space Boussinesq–Cerruti solution.[15,18,25]

Despite enormous discoveries in biochemical-mechanical interplay at the tissue and cell level, the detailed mechano-

[a]*Institute of Biomechanics and Medical Engineering, School of Aerospace Engineering, Tsinghua University, Beijing 10084, People's Republic of China. E-mail: yangchun@tsinghua.edu.cn*
[b]*State Key Laboratory of Membrane Biology, Biodynamic Optical Imaging Centre (BIOPIC), School of Life Sciences, Peking University, Beijing 100871, China*
[c]*Jiangsu Key Laboratory of Medical Optics, Suzhou Institute of Biomedical Engineering and Technology, Chinese Academy of Sciences, Suzhou, Jiangsu 215163, China. E-mail: hui.li@sibet.ac.cn*
[d]*State Key Laboratory for Turbulence and Complex System, and Department of Mechanics and Engineering Science, College of Engineering, Academy for Advanced Interdisciplinary Studies, Peking University, Beijing 100871, People's Republic of China. E-mail: cyxiong@pku.edu.cn*

† Electronic supplementary information (ESI) available: [Fig. S1–S8, Tables S1–S3 (PDF) and Movies S1–S6(MP4). See DOI: https://doi.org/10.1039/d2bm01332k

Published on 22 December 2022. Downloaded by Tsinghua University on 1/9/2023 2:11:16 PM.

transduction mechanism remains poorly understood. The limited spatial resolution of TFM prevents studies on cell traction events at the macromolecular scale. Typical subcellular biomechanical events, such as focal adhesion (FA) turnover and phagocytosis, are several microns to sub-micron in scale,[26,27] comparable to the spatial resolution of fluorescence microscopy, *i.e.*, biochemical signal measuring scale. However, the spatial resolution of the commonly used TFM was above one micron,[28] far from meeting the scale of biomechanical events. Thus, an equal-scale observation technique for cellular biochemical-mechanical coupled information is essential for understanding how cells sense and respond to their surroundings.

The spatial resolution of TFM strongly depends on the sampling interval and the tracking positioning precision of the displacement field vectors. According to the Nyquist criteria, Colin-York *et al.* proposed that the spatial sampling interval must be less than half of any details, which may be resolved in the displacement field.[29] In the past decade, several techniques have been developed to scale down the sampling interval. Stubb *et al.* proposed the fluctuation-based super-resolution TFM method based on super-resolution microscopy enabled by fluorophore intensity fluctuation analysis and reached a sampling interval of 913 nm.[30] Colin-York *et al.* combined stimulated emission depletion (STED) super-resolution microscopy with TFM and obtained a sampling interval of 674 nm.[29] These two methods are still limited in biological applications due to their high time consumption and phototoxicity. Most recently, Barbieri *et al.* combined super-resolution total internal reflection fluorescence structured illumination microscopy (TIRF-SIM) with TFM and established the TIRF-SIM-TFM method.[22] Benefiting from the high spatial temporal resolution and low phototoxicity of SIM (structured illumination microscopy), the TIRF-SIM-TFM method reached a sampling interval of 360 nm and is by far the most promising TFM for biochemical-mechanical coupling investigation. According to the criteria proposed by Colin-York, the optimal traction recovery size was about 720 nm, still larger than the scale of some typical biomechanical events, like nascent focal adhesion turnover. The 360 nm sampling interval is also much larger than the spatial resolution of SIM (about 100 nm), suggesting that the above TFM methods did not make full use of SIM super-resolution imaging. Thus, this bottleneck for improving TFM spatial resolution may not be the spatial resolution of the imaging microscopy. We must think out of the box and try to cut down the displacement sampling interval from a different approach. Since the displacement vectors at the sites where the tracer beads locate can be directly obtained, while the vectors of the other sites must be deduced by interpolation. With a low density of the tracer beads, tiny force signals may be lost as no beads are located nearby. Thus, the bead coating density on the PAAM substrate is crucial not only for a high sampling density but also for the precise positioning of the displacement vectors.

In this article, we propose a modified SIM-TFM with enhanced tracer density, *i.e.*, the enhanced tracer density super-resolution microscopy (ETD-srTFM). We improved the conjugation efficiency between the tracer beads and the PAAM substrate by introducing primary amine groups onto the substrate surface.[31] The bead coating density on the modified PAAM (polyacrylamide) surface reached 15 μm^{-2} for 100 nm diameter beads (the coating interval is 258 nm) and 64 μm^{-2} for 40 nm diameter beads (the coating interval is 125 nm). With a commercial 3-dimensional SIM (3D-SIM), we achieved a displacement sampling interval of 258 nm (comparable to the scale of biomechanical events) and measuring precision of ±56.74 pN (comparable to the rupture force of integrin–ligand bond), thus enabling an equal-scale observation of cellular biochemical-mechanical coupled signals may capture mechanical events at the macromolecular scale. We explored the correlation between the membrane protein trafficking and the traction dynamics in mouse fibroblasts by the fluorescence imaging of paxillin and α5 integrin and synchronized TFM imaging. The results showed that paxillin resided at the same locations with traction, while α5 integrin was located differently, suggesting that these two proteins played different roles in cell adhesion. A time-lapse ETD-srTFM showed a long-term live-cell imaging capacity and a potential for macromolecular mechanical event capturing.

Materials and methods

Substrate preparation, fluorescent beads, and ECM protein coating

We modified a previously published protocol for preparing modified PAAM substrates coated with high-density fluorescent tracer beads and ECM (extracellular matrix) protein.[18,25] Activate glass bottom dishes: glass bottom dishes (In-Vitro-Scientific), ∅ 35 mm dish with ∅ 20 mm glass bottom, were incubated in 0.5% 3-aminopropyltrimethyoxysilane (Sigma Aldrich) for 15 min. After extensive rinsing with ethanol, dishes were incubated in 0.5% glutaraldehyde solution (Beijing Chemical Works) for 30 min, rinsed with DI H_2O, and air-dried.

Stock solutions of 12% acrylamide and 0.3% bis-acrylamide were prepared (Young's modulus 60 kPa). For the modified PAAM substrate, an additional 15 mM (or less, refer to Table S1†) 2-aminoethyl methacrylate hydrochloride (AEMA) (Sigma-Aldrich) was mixed into the PAAM stock solution. For polymerization, 1 μl of 10% ammonium persulfate (Beijing Chemical Works) and 0.1 μl of TEMED (Beijing Chemical Works) were added to 100 μl PAAM stock solution. After thoroughly mixing, the 5 μl mixture was pipetted onto an activated dish and a ∅ 18 mm coverslip was carefully placed on it. The polymerization would be done in 30 min. Then, the top coverslip was peeled off. The thickness of the PAAM substrate was about 30 μm.

The dish was incubated under a 400 μl suspension of 100 nm (1 : 1000, or less, refer to Table S1,† dilution from the 2% stock suspension) or 40 nm (1 : 1000 dilution from the 5% stock suspension) diameter carboxylate yellow-green or red

 This journal is © The Royal Society of Chemistry 2022

Published on 22 December 2022. Downloaded by Tsinghua University on 1/9/2023 2:11:16 PM.

fluorescent microspheres (Thermo Fischer Scientific) for a certain period of time (refer to Table S1†). The dish was incubated in a 250 μl mixture of 1 mg ml^{-1} EDC (Sigma-Aldrich) and 2.5 mg ml^{-1} sulfo-NHS (Sigma-Aldrich) in 50 mM MES, pH 6.0, for 15 min at room temperature. PBS, 2 ml, was added to the dishes and incubated for at least 2 h at room temperature.

The PAAM substrate was incubated in 10 μg ml^{-1} fibronectin using sulfo-SANPAH (Pierce) crosslinker according to a previously published protocol.

Indentation test for PAAM substrate elasticity measuring

Cylindrical PAAM blocks with a size of 20 mm high and 35 mm in diameter were prepared for the indentation test.[32] The formulation of the PAAM substrates was 12% acrylamide and 0.3% bis-acrylamide with or without 15 mM AEMA. An ElectroForce 3100 test instrument with a 3.5 mm diameter spherical indenter was used. The measurements were performed at room temperature (23 °C) and a humidity of about 50%. The displacement controlled loading procedure was applied. The loading rate was set at 0.1 mm s^{-1} and the maximum indentation depth was 2 mm. Hertzain solution was applied to calculate Young's modulus of the PAAM substrate.

Cell culture and cell transfection

Mouse fibroblasts (3t3-Swiss, purchased from National Collection of Authenticated Cell Cultures, Shanghai, China) were cultured at 37 °C in DMEM (Corning) with 10% fetal bovine serum (Gibco) and 1% penicillin–streptomycin at 5% CO_2. For paxillin imaging, 5×10^5 cells were transfected with 5 μg of DNA encoding paxillin-mCherry (a gift from Li Yu, Tsinghua University, Beijing, China) using a Neon Transfection System (Invitrogen), pulse voltage 1350 V, for 20 ms, twice. For integrin α5 imaging, 3×10^5 cells were plated on a 6-well tissue culture plate and transfected with DNA encoding integrin α5-EGFP by a lentivirus transfection system (Cyagen) with a virus concentration of 10 MOI. Twenty-four hours after transfection, cells were digested by trypsin and replated on the PAAM substrates for live-cell imaging.

Cell membrane staining

Mouse fibroblasts (3t3-Swiss) were plated on PAAM substrates coated with or without fluorescent beads for 2 h. The cells were incubated in 5 μM DiI (Thermo Scientific) for 20 min at 37 °C. The cells were fixed with 4% paraformaldehyde for 15 min at room temperature and incubated with DAPI (Sigma-Aldrich) for 15 min before imaging.

Immunofluorescence

Mouse fibroblasts (3t3-Swiss) were plated on PAAM substrates coated with or without fluorescent beads for 2 h. The cells were fixed with 4% paraformaldehyde for 15 min at room temperature, permeabilized with 0.1% Triton X-100 for 5 min, and blocked by 5% bovine serum albumin for 1 h at room temperature. The cells were then incubated with primary antibody against paxillin (1 : 100, Abcam) overnight at 4 °C and Dylight 549-conjugated secondary antibody (1 : 400, EarthOx) for 1.5 h at room temperature, and DAPI (Sigma-Aldrich) for 15 min before imaging.

Atomic force microscopy (AFM) scanning

Before placing the sample on the AFM, it was allowed to equilibrate at room temperature for 10 to 30 min. The sample was kept in a confocal Petri dish, mounted on a magnet, along with a damp KimWipe, until it was ready to be mounted on the AFM. Then, it was rinsed in imaging buffers and mounted on the AFM stage. Avoid shaking while moving the sample. Setting up the experiment: AFM, Bruker bio resolve; probe: Peak Force QNM in Fluid-HiRes-B (tip: 2 nm, k: 0.1 N M^{-1}); software: NanoScope Software version 9.4.

Confocal and SIM microscope setting up

SIM imaging was performed using the Nikon N-SIM system with a 100× NA 1.49 TIRF objective lens and an EMCCD (Andor iXon DU-897). The laser power was set at 20% and the exposure time was 20 ms for 488 nm and 561 nm channels. The pixel size of the SIM super-resolution images was 30 nm. Confocal imaging was performed using a Nikon A1 confocal system with a 100× NA 1.40 objective lens. The laser power was set at 2% for the 488 nm and 561 nm channels (Table S2†).

The theoretical standard deviation of the point spread function (PFS) calculation

The standard deviation σ of SIM PSF was calculated as follows: according to the diffraction theorem, the spatial resolution of an optical microscope is about $\Delta_{xy} = 0.61\lambda_0/\mathrm{NA}$. The emission wavelength of green fluorescent beads is about λ_0 = 500 nm and the numerical aperture (NA) of the objective lens is NA = 1.49. The spatial resolution was calculated to be Δ_{xy} = 204.7 nm. This value is equivalent to the full width at half maximum (FWHM) of PSF and the standard deviation of PSF can be calculated by σ = FWHM/2.355. The spatial resolution of SIM is about half of that of a traditional optical microscope, and the pixel size of SIM was 30 nm. Thus, the theoretical standard deviation of SIM PSF was calculated to be σ = 1.44 pixels.

Displacement field tracking

The particle tracking velocimetry (PTV) algorithm, calculating the displacement field, was modified from a published protocol for high-resolution TFM.[18]

The filtering and fitting window size was set at 4σ, since it can contain more than 95% of the bead imaging pattern and avoid the interaction of the adjacent beads. We also used a simulating program to confirm that 4σ is an optimized choice to ensure the accuracy of displacement tracking and traction reconstruction (Fig. S2†). The detailed description of the simulating program will be described in the next subsection and the figure legend of Fig. S2.†

The displacement tracking procedure is as follows (Matlab built-in functions are in *italics*): (1) we used *normxcorr2* to calculate the image correlation coefficients between the reference

Published on 22 December 2022. Downloaded by Tsinghua University on 1/9/2023 2:11:16 PM.

and the deformed bead images, and eliminated the stage shift between these two images. (2) The initial standard deviation of the point spread function (PSF) was set as the theoretical PSF standard deviation calculated above (σ = 1.44 pixels for ETD-srTFM or according to the imaging conditions, refer to Table S2†), and *fspecial* and *imfilter* were used to perform Laplacian Gaussian filtering on the reference bead image (the filtering window size is set at 4σ) and the filtering image is named as *imgLoG*. (3) Ordfilt2 was used to perform maximum filtering on *imgLoG* (the filtering window size is set at 2σ), and the filtered image is named as *imgMax*. (4) We compared *imgLoG* and *imgMax*, and the points with the same value as the candidate centre position of the tracer beads were picked. (5) *Lsqcurvefit* was used to fit a 2D Gaussian function at each candidate bead (the window size was set at 4σ), and the fluorescent intensity, the centre position, the standard deviation, and the fitting residual were recorded. (6) The beads with fitting residuals much larger than the average value were eliminated (exceeding the 95% confidence interval of the beads fitting residual distribution). (7) Rosin threshold was used to eliminate the beads with fluorescent intensity significantly lower than the general level.[33] (8) Windows on top of each recognized bead (the window size is set at 4σ) were placed and the correlation coefficient matrix between each window in the reference image and the corresponding region in the deformed image was calculated. The displacement of each bead was calculated by finding the peak value in the correlation coefficient matrix. (9) Subpixel displacements could be calculated by a 2-dimensional Gaussian fitting to the correlation coefficient matrix.

Traction field reconstruction, simulation, and regularization parameter optimization

The PAAM substrate shows a homogeneous, isotropic, and linear elastic behaviour, and the substrate thickness is much larger than the lateral dimension of the cell and the displacement. Thus, the displacement field u can be calculated from the traction field f by:

$$u_i(x) = \int \sum_j G_{ij}(x - x')f_j(x')\mathrm{d}x', \quad (1)$$

where G is the Boussinesq Green function.[34] An early approach to calculate the traction from the measured displacement field was to solve the inversion of eqn (1) in real space,[13] which was quite computationally demanding. The now widely used the Fourier transform traction cytometry (FTTC) method was used to solve eqn (1) in Fourier space,[15] transforming the convolution into a simple product, which significantly improves the efficiency and reliability of the algorithm. Introducing appropriate regularization schemes into FTTC can further improve the resolution of TFM.[17] We chose Tikhonov regularized FTTC to calculate the traction field in ETD-srTFM.[15,17]

The regularization parameter λ should be optimized to improve the accuracy of the traction field reconstruction.[21] We designed a MatLab program to simulate the imaging and calculation process of ETD-srTFM to examine the effect of regularization: (1) imitating the size of common adhesion spots and their arrangement in a cell, a simulated traction field was set, as shown in Fig. S1A.† The magnitude of the traction was distributed spatially and uniformly in the red ellipses with a length of 2 μm, a width of 0.5 μm, and an interval of 1 μm. The direction of the tractions was uniformly pointed to the right side. (2) The Boussinesq–Cerruti solution was used to calculate the simulated displacement field. (3) A PAAM substrate surface coated with beads was simulated at a density of 15 μm^{-2}. (4) The simulated displacement field was substituted and beads positions were calculated after the substrate deformation. (5) The simulated beads images were convolved with a PSF (point spread function) of SIM and superimposed with 5% white noise. (6) The displacement field was calculated with PTV. (7) Reg-FTTC with different λ was used to calculate the reconstructed traction field (Fig. S1A†).

The PSF standard deviation of ETD-srTFM obtained by the Gaussian fitting was about 1.5 pixels, slightly larger than the theoretical value of 1.44 pixels. Such differences may be caused by the background noise of the microscope light path and the camera and can be corrected by introducing white noise into the images of the simulated beads. Therefore, we chose σ = 1.44 pixels for the ETD-srTFM simulation.

We used two parameters to judge the reconstruction effect of the traction field,[21] the traction detection ability $\psi = \|\bar{f}_{\mathrm{reconstr}}\|_{@A_0}/\max(\|f_{\mathrm{reconstr}}\|_{@A_{\mathrm{background}}})$ (*i.e.*, the average value of the reconstructed traction magnitude at A_0 divided by the maximum value of the reconstructed traction magnitude at $A_{\mathrm{background}}$) and the traction field residual $\zeta = \|f_{\mathrm{reconstr}} - f_0\|_2$. Among them, f_0 is the simulated traction field, f_{reconstr} is the reconstructed traction field, A_0 is the position with traction locates (*i.e.*, the red ellipse regions in the top view of Fig. S1A†) and $A_{\mathrm{background}}$ is the position with no traction was located (*i.e.*, the blue region in the top view of Fig. S1A†).

The results showed that when the regularization parameter was set at $\lambda = 3 \times 10^{-8}$, the traction force recognition ability ψ was maximized, the traction force residual ζ was minimized, and the traction force field contour map was visually almost identical to the simulated traction field (Fig. S1B and C†). Therefore, we chose $\lambda = 3 \times 10^{-8}$ as the regularization parameter of ETD-srTFM.

Quantitative estimation of traction field spatial resolution

The simulation program described in the previous subsection was also used to estimate the spatial resolution of ETD-srTFM (Fig. S3†). The input-simulated traction maps are shown at the top. The length and the width of the red ellipses here were set to 2 μm and 0.4 μm, respectively. We changed different intervals of the red ellipse regions, mimicking traction distributions in step 1 and running through steps (1) to (7). The simulated bead density was set to either 10 or 15 μm^{-2}. The corresponding traction field results are shown in Fig. S3.† A traction map is considered to be resolvable by the ETD-srTFM if the output traction field can be distinguished as three distinct spots and not blur into one another. The result shows that the traction resolution strongly depends on the bead

 This journal is © The Royal Society of Chemistry 2022

Published on 22 December 2022. Downloaded by Tsinghua University on 1/9/2023 2:11:16 PM.

density, *i.e.*, the displacement sampling interval of the TFM methods. ETD-srTFM with a 15 μm^{-2} bead density can resolve traction with a 500 nm interval, while the 10 μm^{-2} bead density can only resolve a 700 nm interval. Thus, the traction resolution of ETD-srTFM was about 500 nm.

Results

PAAM substrate surface modification significantly improves the tracer bead coating density

The conventional TFM method uses an EDC two-step reaction to crosslink the carboxylate-modified beads with the amino groups on the PAAM surface. The amino groups on the PAAM surface are amide groups with low nucleophilicity, resulting in a limited crosslinking efficiency between the beads and the PAAM substrate. Under the conventional crosslinking conditions, the bead density was only 1.77 μm^{-2} for 100 nm beads and 2.18 μm^{-2} for 40 nm beads. Increasing the bead concentration and prolonging the sedimentation time could, to some extent, improve the bead density. The 100 nm bead density was limited to 5 μm^{-2} and the sampling interval was 447 nm under such conditions (Fig. 1A–C and Table S1†). To improve the cross-linking efficiency of the beads, we must modify the surface property of the PAAM substrate.

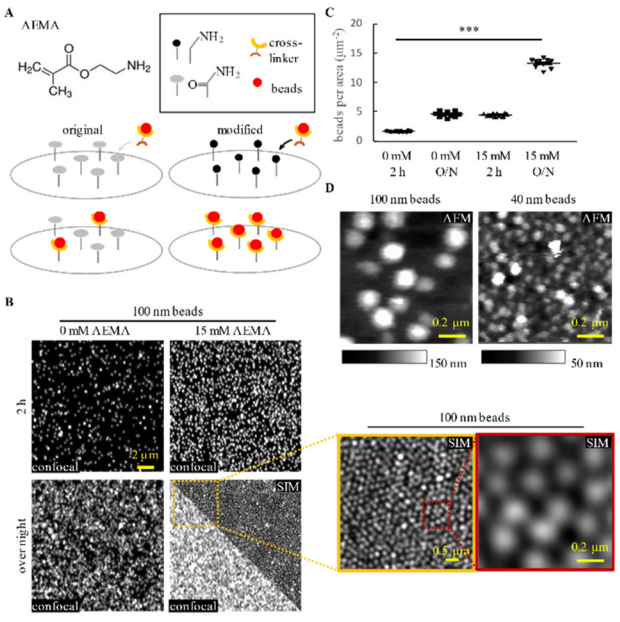

Fig. 1 AEMA modification can greatly improve the bead coating density on the surface of the PAAM substrate. (A) Schematic of AEMA modification. AEMA introduced primary amino groups to the PAAM surface, increasing crosslinking efficiency and bead coating density. (B) Representative confocal or SIM images of 100 nm green fluorescent beads coated with different sedimentation time on the PAAM surface with or without AEMA modification. (C) Statistics of 100 nm bead sampling density in (B) identified by 2D Gaussian fitting. (O/N, overnight; ***, one way ANOVA, $p < 0.001$) (D) AFM images of the 100 nm or 40 nm beads coated PAAM surface morphology. Gray scale value stands for height.

We added 2-aminoethyl methacrylate hydrochloride (AEMA) to the PAAM stock solution, transforming the amide groups on the PAAM surface into primary amino groups and increasing the crosslinking efficiency without changing the mechanical properties of the material (Fig. 1A and Fig. S4†). The 100 nm bead density was about 15.03 μm^{-2} after the surface modification (the PAAM stock solution containing 15 mM AEMA), and the sampling interval was about 258 nm (Fig. 1B and C). Under such conditions, the beads were unable to be distinguished by confocal microscopy. To generalize the application of TFM at different measuring scales, we used three parameters (the AEMA concentration, the bead concentration, and the sedimentation time) for different bead coating densities. The 100 nm bead density could be modulated from 0.58 μm^{-2} to 15.03 μm^{-2}, meeting the need for both conventional and super-resolution traction measurements (Table S1†). Stimulated emission depletion microscopy (STED) and atomic force microscopy (AFM) showed that AEMA modification could also improve the coating density of 40 nm beads to 64 μm^{-2} (the sampling interval was about 125 nm, comparable to the SIM resolution) (Fig. 1D and Fig. S5†). Thus, the AEMA-modified PAAM substrate can significantly increase the tracer bead coating density, which is crucial for super-resolution traction measurement.

High-density tracer beads imaging and displacement calculation for a novel super-resolution TFM method

By introducing the AEMA-modified PAAM substrate with extremely dense tracer beads, we attempted to establish a new super-resolution TFM method, called enhanced tracer density super-resolution TFM (ETD-srTFM). Previous studies have proved that super-resolution microscopy was recommended for improving the spatial resolution for recovering traction. Due to its low phototoxicity and not requiring special fluorescence labelling, SIM is more suitable for live-cell imaging. We chose a ready-to-use commercial SIM system for ETD-srTFM imaging.

The spatial resolution of TFM strongly depends on the sampling interval and the tracking positioning precision of the displacement field. In addition to the high bead coating density, the bead positioning precision of SIM-TFM is challenging. Since the SIM reconstruction algorithm is an ill-posed deconvolution problem, SIM requires a strong fluorescence intensity for the samples.[35] The 40 nm beads have relatively weak fluorescent intensity, leading to reconstruction artifacts in the SIM image. Some previous studies chose particle image velocimetry (PIV) for the substrate displacement tracking to reduce the effect of the artifacts.[22,36] By splitting the image into rectangular windows and calculating the displacement of each window, the PIV method may encounter empty windows and result in tracking errors, since the tracer beads scatter randomly. To avoid such errors, PIV usually requires a proper window size to guarantee more than one bead in each window, drawing back the benefits of dense bead coating and resulting in a loss of displacement sampling capacity. Comparatively, the 100 nm beads exhibited a higher quality SIM image

Published on 22 December 2022. Downloaded by Tsinghua University on 1/9/2023 2:11:16 PM.

(Fig. S6†), *i.e.*, each bead can be easily distinguished from the background. Under such conditions, particle tracking velocimetry (PTV) is a preferable choice for the bead displacement calculating.[17,18,21] Displacement fields obtained by these two algorithms showed that PTV produced a displacement field with higher quality and a higher signal-to-noise ratio than PIV (Fig. S7†). AFM confirmed that the bead coating density on the PAAM substrate containing 15 mM AEMA was about 15 μm^{-2}, indicating that the SIM microscopy and PTV algorithm was preferable to distinguish individual beads at this density (Fig. 1D and Fig. S7†). Thus, we employed 100 nm bead-coated PAAM substrates and a PTV displacement tracking algorithm for ETD-srTFM.

The ETD-srTFM method can resolve traction details 258 nm apart

To evaluate the traction detectability of ETD-srTFM, we investigated the sampling density and positioning precision of the displacement field. We prepared six PAAM substrates with different bead coating densities and captured 100 frames of each sample with confocal or SIM microscopy at an interval of 5 s. The pixel sizes of both microscopies were set at 30 nm. We determined the centre of each bead by 2D Gaussian fitting and calculated the identified bead density and the standard deviation of the bead positions in the 100 frames (*i.e.*, the positioning precision of each bead). The results showed that the sampling capacity of the confocal was equal to the SIM when the coating density was low and dropped significantly when the coating density gradually increased, and the bead detectability of the confocal dropped (Fig. 2A). The confocal was unable to recognize each bead when the bead density reached 15 μm^{-2} Bead positioning precision was primarily determined by the type of microscopy. The positioning precisions of confocal and SIM were ±10.9 nm and ±1.75 nm, respectively.

To assess the error brought by trypsin treatment, we performed each step of ETD-srTFM and confocal-TFM (with sparse bead density, about 2 μm^{-2}) without plating cells on the substrate, captured the bead images before and after the trypsin treatment and tracked the substrate displacement (marked as $\Delta u = \{(x_1,y_1),(x_2,y_2),...,(x_n,y_n)\}$, n is the tracked displacement bead number). We put together the x components and the y components of the tracked displacement vectors and draw a histogram (*i.e.*, the abscissa of the histogram is the following set: $\{x_1,x_2,...,x_n,y_1,y_2,...,y_n\}$). The results showed that the displacement components present a Gaussian distribution with a standard deviation of about ±1.72 nm for ETD-srTFM and ±11.1 nm for confocal-TFM (Fig. 2B and Table S2†).

We assessed the traction detectability of ETD-srTFM based on the Boussinesq–Cerruti theory[37] (Fig. 2C). As a tangential concentrated force P was applied to O on the substrate surface, the displacement u at O' should be: $u(x,0,0) = P(1+\nu)/(\pi Ex)$, where E and ν are the Young's modulus and Poisson's ratio of the substrate. When the bead coating density was 15 μm^{-2}, the displacement sampling interval of ETD-srTFM was about 258 nm. Considering the displacement measurement precision ±1.75 nm and typical PAAM constitutive parameters, we determined the parameters in the above equation as x = 258 nm, u = 1.75 nm. E = 60 kPa and ν = 0.5. The minimum detectable force was calculated as 56.74 pN (*i.e.*, the traction measuring precision was ±56.74 pN), comparable to the rupture force of the integrin–ligand bond (about 100 pN),[38] suggesting that ETD-srTFM is capable to capture macromolecular mechanical events. On the contrary, the measuring precision of confocal-TFM was about ±1057 pN, much larger than the bond rupture force (Fig. 2D and Table S2†).

Thus, an AEMA-modified PAAM substrate can bring an overall promotion of bead sampling density and positioning precision, leading to an effective improvement in displacement tracking accuracy and breaking through the bottleneck of the super-resolution TFM method.

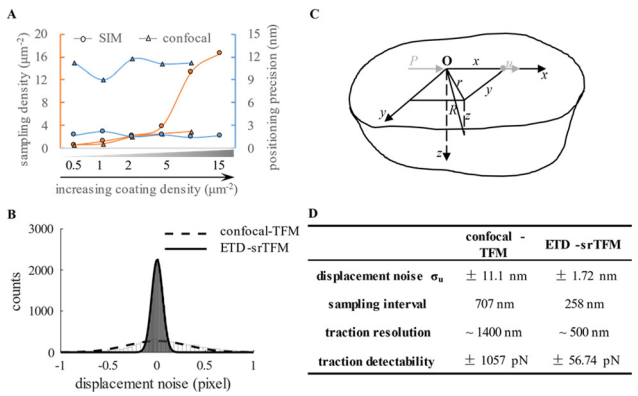

Fig. 2 Error estimation of ETD-srTFM. (A) Bead sampling density and positioning precision on the PAAM substrate identified by 2D Gaussian fitting. The abscissa represents six independent samples prepared by different experimental conditions (Table S1,† sample number: 1, 2, 4, 5, 8, 9). (B) Displacement errors brought by trypsin treatment. Histogram of the displacement vectors by tracking the beads on a substrate with no cell plating. Solid and dashed lines are Gaussian fittings. (C) Schematic of Boussinesq–Cerruti solution. (D) Error estimation of confocal-TFM and ETD-srTFM.

The accurate traction field measured by ETD-srTFM shows a high correlation with the paxillin location

We used mouse fibroblasts (3t3-Swiss cell line) to investigate the biological application prospects of ETD-srTFM. Immunofluorescence staining showed that the spreading area and FA (focal adhesion) formation of fibroblasts were not affected by the densely coated beads on PAAM substrates (Fig. S8†).

Fibroblasts expressing paxillin-mCherry to mark FAs were plated on the modified PAAM substrates (Young's modulus 60 kPa, bead density 15 μm^{-2}) for 2 h. The traction field detected by ETD-srTFM was highly correlated to FA distribution (Fig. 3A).

To validate that higher bead sampling density can improve traction field measuring accuracy, sparse bead sampling rates (5, 2, or 0.5 μm^{-2}) were imitated by randomly removing part of the beads from the original SIM beads image. We then refilled the displacement vectors of the removed beads by interpolation and calculated the traction field using the same grid

 This journal is © The Royal Society of Chemistry 2022

Published on 22 December 2022. Downloaded by Tsinghua University on 1/9/2023 2:11:16 PM.

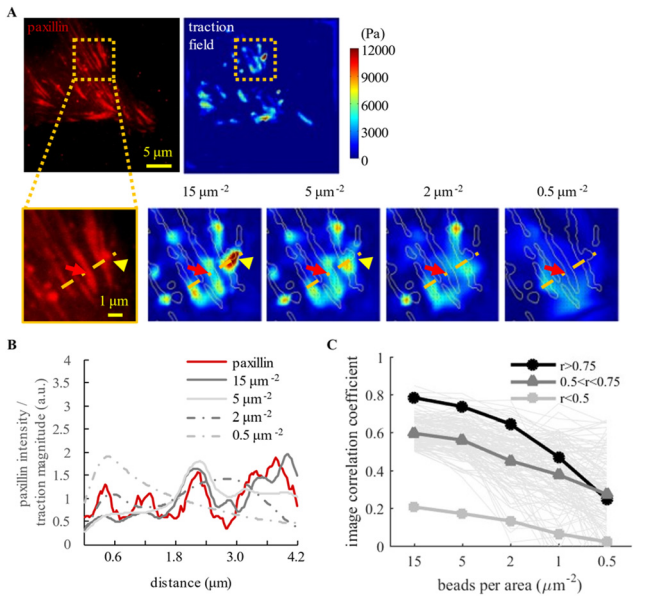

Fig. 3 High-sampling density can significantly improve the traction filed measuring accuracy. (A) Representative paxillin images and traction field measured by ETD-srTFM. Zoomed views of the region framed by the yellow dashed line and the traction fields of the imitated sparse sampling images are shown in the bottom. (B) The paxillin intensity and the traction magnitude profiles from the indicated yellow dashed line in the bottom view of (A). (C) The image correlation coefficients between the paxillin intensity and the traction magnitude in FAs (focal adhesions) and their vicinity change with the sampling density. Otsu thresholding was applied to pick out the FAs in a paxillin image, and the range of 5 μm around each FA was defined as its neighbouring region. The thick lines show the average value of the high, the medium or the low correlated group. The thin lines represent each individual FA. For clarity, only the high and the medium correlated group FAs are presented.

size and regularization parameter (Fig. 3A). The detail of strong local traction indicated by ETD-srTFM (yellow arrow) was missed when the bead sampling density dropped to 5 μm^{-2}. The traction magnitude and paxillin intensity showed a nearly consistent change along the grey-dashed line (perpendicular to the long axis of the FAs in Fig. 3A) at high sampling density, where the distribution of traction and paxillin showed a significantly different pattern when the bead sampling density dropped to 0.5 μm^{-2} (Fig. 3B). We calculated the image correlation coefficient (denoted by r) between paxillin intensity and traction magnitude in each FA and its neighbouring region (Fig. 3C). The Fas were classified into three groups according to the r calculated from the 15 μm^{-2} bead image ($r \geq 0.75$, high correlated group; $0.5 \leq r < 0.75$, medium correlated group; $r < 0.5$, low correlated group). A significant decrease in the correlation coefficients was observed as the sampling density reduced, especially in the highly correlated group. The red arrow showed an FA with two local traction maxima which were not detected by low-density sampling, suggesting that the adhesion is discontinuous in this FA (Fig. 3A).

The above results demonstrate that higher bead sampling density can improve traction field measuring accuracy, and the traction distribution of a fibroblast shows a high correlation with its paxillin location.

To test whether ETD-srTFM has the potential for capturing macromolecular mechanical events, we performed time-lapse live-cell imaging. We plated paxillin-mCherry 3t3-Swiss cells on a PAAM substrate coated with fluorescent beads and fibronectin for 2 h. The cells were imaged for about 5 min at intervals of 10 s (Fig. 4 and Movies 1, 2†). The displacement of a single bead (yellow circle) showed a transient movement as paxillin passed by. Correspondingly, the local traction at this position increased continuously and was followed by a vertiginous drop. The magnitude of this traction variation was about 300 pN, *i.e.*, three times the rupture force of the integrin–ligand bond, suggesting that ETD-srTFM had a potential for macromolecular mechanical events capturing.

Integrin α5 manipulates cell–matrix conjunction but not direct traction transmission

Integrin α5 is highly expressed in fibroblasts and participates in fibrillogenesis.[39–41] To investigate the relationship between integrin α5 turnover and cell traction, integrin α5-EGFP transfected 3t3-Swiss cells were plated on a PAAM substrate coated with fluorescent beads and fibronectin for 2 h and imaged for about 20 min at intervals of 2.5 min (Fig. 5A and Movies 3–6†).

We focused on lamellipodium regions where integrin turnover was dynamic. In protruding lamellipodia, cell traction appeared early at the front of the cell edge and extended forward as the cells protruded, but integrin α5 could not be observed in this area (Movies 3 and 4†). In retracting lamellipodia, integrin α5 gathered and cell traction could be seen,

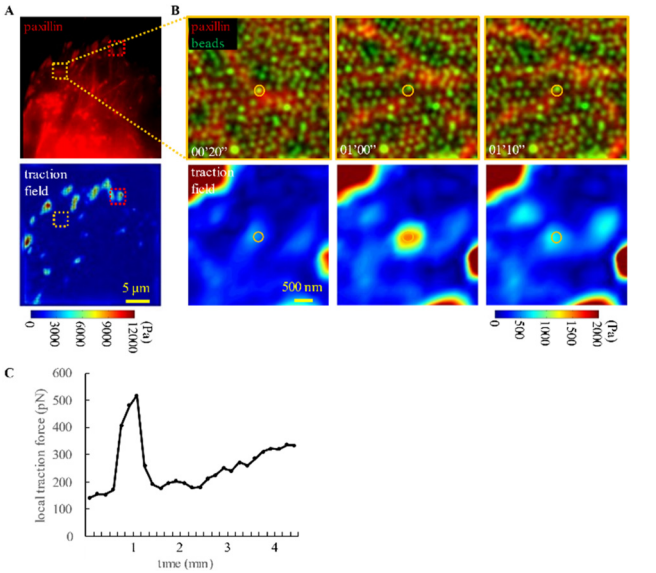

Fig. 4 The ETD-srTFM imaging capture macromolecular mechanical events. (A) Representative movie screenshots of the paxillin-mCherry transfected 3t3-Swiss cells and the corresponding traction fields (snapshots of Movie S1†). (B) Zoomed views of the region framed by the yellow dashed line in (A) (snapshots of Movie S2†). (C) Local traction force at the position indicated by yellow circle in (B).

Published on 22 December 2022. Downloaded by Tsinghua University on 1/9/2023 2:11:16 PM.

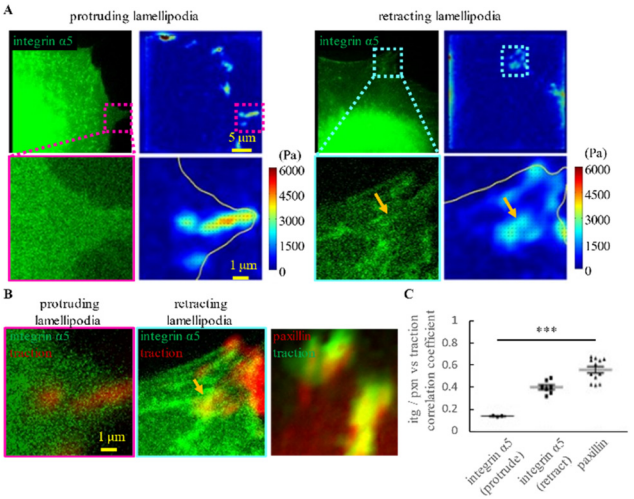

Fig. 5 Integrin α5 aggregates in retracting lamellipodia and is not mainly responsible for cell anchorage. (A) Top view: representative movie screenshots of the integrin α5-EGFP transfected 3t3-Swiss cells and the corresponding traction fields (snapshots of Movies S3 and S5†). Bottom view: zoomed views of the regions framed by the magenta/cyan dashed line (snapshots of Movies S4 and S6†). (B) Time-stack max intensity projections of proteins, integrin α5 (zoomed region framed by the magenta/cyan dashed line in (A)) or paxillin (zoomed region framed by the red dashed line in (Fig. 4A)), and the traction fields in the lamellipodia. (C) Image correlation coefficients of the max intensity projections between the proteins, integrin α5 or paxillin, and the cell tractions in the lamellipodia (***, one way ANOVA, $p < 0.001$).

while their distributions were significantly different. Cell traction was located proximal to the cell edge compared with integrin α5 (Fig. 5). These results suggested that integrin α5 is not mainly responsible for the anchorage of the cells.

We analysed the dynamic relationship between integrin α5 distribution and cell traction and found that they moved along the same direction in the retracting lamellipodia (Fig. 5A, B and Movie 6†). Notice the position indicated by the yellow arrow where integrin α5 aggregated and was followed by high traction. This result suggested that the integrin α5 turnover in the retracting lamellipodia guides the cell–matrix adhesion afterwards. We used time-stack max intensity projection to quantify the relationship between integrin α5 distribution and cell traction (Fig. 5B). In the retracting lamellipodium, the green and red lines revealed the trajectories of integrin α5 and traction, respectively. These two trajectories extended in the same direction and overlapped at the position indicated by the yellow arrow. We calculated the correlation coefficient of the projection images between proteins (integrin α5 or paxillin) and cell traction. The trajectory of integrin α5 was higher correlated with cell traction in the retracting lamellipodia than in the protruding lamellipodia, while paxillin showed the highest correlation with traction (Fig. 5C). Since integrin α5 participates in fibrillogenesis and ECM remodelling, we supposed that integrin α5 modulated the remodelling of ECM by guiding cell–matrix adhesion in the posterior region of the migrating cell rather than by traction transmission.

Discussion

TFM is one of the most powerful approaches for measuring cellular or subcellular mechanical signals, however, macromolecular mechanical measurements remain challenging. In the past decade, several super-resolution TFM methods have been proposed by introducing super-resolution imaging techniques (STED or SIM).[22,29,42,43] The minimum displacement sampling interval achieved by TIRF-SIM-TFM is 360 nm, nevertheless, much larger than the spatial resolution of SIM (about 100 nm). We suggest that this bottleneck in improving TFM spatial resolution is not the spatial resolution of the microscope for imaging but the sampling density of fluorescent tracer beads. Here, we proposed a method to modify the PAAM substrate surface by increasing the bead sampling density to 15 μm^{-2} for 100 nm beads (the bead sampling interval is 258 nm) and 64 μm^{-2} for the 40 nm bead (the bead sampling interval is 125 nm). Tracer bead positioning precision is another crucial element for high-resolution tracer beads sampling followed by macromolecular scale traction measurement. Since the ready-to-use commercial SIM in ETD-srTFM is a mechanical grating-based linear SIM system, 100 nm beads are recommended to guarantee a high signal-to-noise ratio for imaging and precise bead positioning, despite sacrificing certain sampling density. If a liquid crystal spatial light modulator (LC-SLM) based nonlinear SIM system is employed in ETD-srTFM,[44] 40 nm beads can be used and the displacement sampling interval is supposed to reach 125 nm, almost equivalent to the spatial resolution of SIM. Thus, our PAAM surface modification method can make good use of SIM, breaking through the bottleneck of super-resolution TFM, and propel the spatial resolution of traction measurement to a macromolecular scale, comparable to biochemical signal imaging.

We introduced AEMA modification to increase the cross-linking efficiency between tracer beads and the PAAM substrate without changing the mechanical properties of the material. This modification method not only improves the bead coating density but also modulates the coating density by changing the AEMA concentration and experimental conditions. The AEMA-modified PAAM substrate can be applied to a wide range of traction measuring scales (from macromolecular to collective cell migration). We provide recommended experimental and computational parameters for different traction measuring scales in Table S2.† Thus, AEMA modification can produce a ready-to-use widely applicable TFM method of reliable quality for mechanobiology research.

Conclusions

In this article, we proposed a method to modify the PAAM substrate surface, significantly increasing the bead coating density to 15 μm^{-2} for 100 nm beads and 64 μm^{-2} for 40 nm beads. The ETD-srTFM method was established based on this substrate modification method and PTV (particle tracking velocimetry), achieving a sampling interval of 258 nm, comparable

 This journal is © The Royal Society of Chemistry 2022

Published on 22 December 2022. Downloaded by Tsinghua University on 1/9/2023 2:11:16 PM.

to some typical mechanobiology events, such as nascent focal adhesion overturn and vesicle internalization. The traction measuring precision is ±56.74 pN, comparable to the rupture force of the integrin–ligand bond. Combined with live-cell imaging, ETD-srTFM was proved suitable for biochemical-mechanical coupling measurement. Benefiting from this approach, we investigated the relationship between protein trafficking and traction dynamics. Paxillin residence highly correlated with traction, whereas integrin α5 showed a different positioning with traction, suggesting that integrin α5 is not mainly responsible for cell anchorage. Taken together, ETD-srTFM has broken through the bottleneck of super-resolution TFM techniques and may shed light on mechanotransduction research at the macromolecular scale.

Author contributions

Yue Xu: conceptualization, methodology, investigation, writing – original draft. Chuanwen Guo: methodology, investigation. Xueyi Yang: investigation. Weihong Yuan: investigation. Xu Zhang: investigation. Yujie Sun: supervision. Gang Wen: methodology. Linbo Wang: methodology. Hui Li: supervision, writing – review, and editing. Chunyang Xiong: supervision. Chun Yang: supervision, conceptualization, writing – review and editing.

Conflicts of interest

There are no conflicts to declare.

Acknowledgements

We thank the National Centre for Protein Sciences at Peking University in Beijing, China, particularly Dr Siying Qin for technical help with AFM. This work was financially supported by National Nature Science Foundation of China no. 11972214.

References

1 G. Charras and E. Sahai, *Nat. Rev. Mol. Cell Biol.*, 2014, **15**, 813–824.
2 T. Iskratsch, H. Wolfenson and M. P. Sheetz, *Nat. Rev. Mol. Cell Biol.*, 2014, **15**, 825–833.
3 J. T. Parsons, A. R. Horwitz and M. A. Schwartz, *Nat. Rev. Mol. Cell Biol.*, 2010, **11**, 633–643.
4 S. V. Plotnikov, A. M. Pasapera, B. Sabass and C. M. Waterman, *Cell*, 2012, **151**, 1513–1527.
5 A. J. Engler, S. Sen, H. L. Sweeney and D. E. Discher, *Cell*, 2006, **126**, 677–689.
6 V. Jaumouille, A. X. Cartagena-Rivera and C. M. Waterman, *Nat. Cell Biol.*, 2019, **21**, 1357–1369.
7 J. Wang, F. Lin, Z. Wan, X. Sun, Y. Lu, J. Huang, F. Wang, Y. Zeng, Y.-H. Chen, Y. Shi, W. Zheng, Z. Li, C. Xiong and W. Liu, *Sci. Signaling*, 2018, **11**, eaai9192.
8 X. Wang and T. Ha, *Science*, 2013, **340**, 991–994.
9 Y. Zhang, C. Ge, C. Zhu and K. Salaita, *Nat. Commun.*, 2014, **5**, 5167.
10 H. Li, C. Zhang, Y. Hu, P. Liu, F. Sun, W. Chen, X. Zhang, J. Ma, W. Wang, L. Wang, P. Wu and Z. Liu, *Nat. Cell Biol.*, 2021, **23**, 642–651.
11 P. Roca-Cusachs, V. Conte and X. Trepat, *Nat. Cell Biol.*, 2017, **19**, 742–751.
12 A. K. Harris, P. Wild and D. Stopak, *Science*, 1980, **208**, 177–179.
13 M. Dembo and Y.-L. Wang, *Biophys. J.*, 1999, **76**, 2307–2316.
14 J. Robert, J. Pelham and Y.-L. Wang, *Mol. Biol. Cell*, 1999, **10**, 935–945.
15 J. P. Butler, I. M. Tolić-Nørrelykke, B. Fabry and J. J. Fredberg, *Am. J. Physiol.: Cell Physiol.*, 2002, **282**, C595–C605.
16 U. S. Schwarz, N. Q. Balaban, D. Riveline, A. Bershadsky, B. Geiger and S. A. Safran, *Biophys. J.*, 2002, **83**, 1380–1394.
17 B. Sabass, M. L. Gardel, C. M. Waterman and U. S. Schwarz, *Biophys. J.*, 2008, **94**, 207–220.
18 S. V. Plotnikov, B. Sabass, U. S. Schwarz and C. M. Waterman, in *Methods in Cell Biology*, ed. J. C. Waters and T. Wittman, Academic Press, 2014, vol. 123, pp. 367–394.
19 Y. Zhao, K. Pal, Y. Tu and X. Wang, *J. Am. Chem. Soc.*, 2020, **142**, 6930–6934.
20 J. M. Brockman, H. Su, A. T. Blanchard, Y. Duan, T. Meyer, M. E. Quach, R. Glazier, A. Bazrafshan, R. L. Bender, A. V. Kellner, H. Ogasawara, R. Ma, F. Schueder, B. G. Petrich, R. Jungmann, R. Li, A. L. Mattheyses, Y. Ke and K. Salaita, *Nat. Methods*, 2020, **17**, 1018–1024.
21 S. J. Han, Y. Oak, A. Groisman and G. Danuser, *Nat. Methods*, 2015, **12**, 653–656.
22 L. Barbieri, H. Colin-York, K. Korobchevskaya, D. Li, D. L. Wolfson, N. Karedla, F. Schneider, B. S. Ahluwalia, T. Seternes, R. A. Dalmo, M. L. Dustin, D. Li and M. Fritzsche, *Nat. Commun.*, 2021, **12**, 2169.
23 Y.-L. Wang and R. J. Pelham, in *Methods in Enzymology*, Academic Press, 1998, vol. 298, pp. 489–496.
24 K. Liu, Y. Yuan, J. Y. Huang, Q. Wei, M. S. Pang, C. Y. Xiong and J. Fang, *PLoS One*, 2013, **8**, 11.
25 Y. Xu, J. Li, S. Zhou, X. Tang, Y. Zhang, F. Lin, C. Xiong and C. Yang, *ACS Biomater. Sci. Eng.*, 2017, **3**, 2987–2998.
26 B. Wehrle-Haller and B. A. Imhof, *Trends Cell Biol.*, 2002, **12**, 382–389.
27 R. S. Flannagan, V. Jaumouille and S. Grinstein, in *Annual Review of Pathology: Mechanisms of Disease, Vol 7*, ed. A. K. Abbas, S. J. Galli and P. M. Howley, Annual Reviews, Palo Alto, 2012, vol. 7, pp. 61–98.
28 H. Colin-York and M. Fritzsche, *Curr. Opin. Biomed. Eng.*, 2018, **5**, 1–5.
29 H. Colin-York, D. Shrestha, J. H. Felce, D. Waithe, E. Moeendarbary, S. J. Davis, C. Eggeling and M. Fritzsche, *Nano Lett.*, 2016, **16**, 2633–2638.

Published on 22 December 2022. Downloaded by Tsinghua University on 1/9/2023 2:11:16 PM.

30 A. Stubb, R. F. Laine, M. Miihkinen, H. Hamidi, C. Guzman, R. Henriques, G. Jacquemet and J. Ivaska, *Nano Lett.*, 2020, **20**, 2230–2245.
31 S. Lee, A. E. Stanton, X. M. Tong and F. Yang, *Biomaterials*, 2019, **202**, 26–34.
32 M.-G. Zhang, Y.-P. Cao, G.-Y. Li and X.-Q. Feng, *Biomech. Model. Mechanobiol.*, 2014, **13**, 1–11.
33 P. L. Rosin, *Pattern Recognit.*, 2001, **34**, 2083–2096.
34 L. D. Landau and E. M. Lifshitz, *Theory of Elasticity*, Pergamon, Oxford, 1986.
35 J. Demmerle, C. Innocent, A. J. North, G. Ball, M. Muller, E. Miron, A. Matsuda, I. M. Dobbie, Y. Markaki and L. Schermelleh, *Nat. Protoc.*, 2017, **12**, 988–1010.
36 K. A. Beningo, M. Dembo, I. Kaverina, J. V. Small and Y. L. Wang, *J. Cell Biol.*, 2001, **153**, 881–887.
37 Y. Y. Kagan, *J. Geophys. Res.: Solid Earth Planets*, 1988, **93**, 10560–10574.
38 L. Jiang, Z. L. Sun, X. F. Chen, J. Li, Y. Xu, Y. Zu, J. L. Hu, D. Han and C. Yang, *ACS Nano*, 2016, **10**, 207–217.
39 E. Cukierman, R. Pankov, D. R. Stevens and K. M. Yamada, *Science*, 2001, **294**, 1708–1712.
40 Y. Su, W. Xia, J. Li, T. Walz, M. J. Humphries, D. Vestweber, C. Cabanas, C. F. Lu and T. A. Springer, *Proc. Natl. Acad. Sci. U. S. A.*, 2016, **113**, E3872–E3881.
41 M. Benito-Jardon, S. Klapproth, I. Gimeno-Lluch, T. Petzold, M. Bharadwaj, D. J. Muller, G. Zuchtriegel, C. A. Reichel and M. Costell, *eLife*, 2017, **6**, e22264.
42 H. Colin-York, C. Eggeling and M. Fritzsche, *Nat. Protoc.*, 2017, **12**, 783–796.
43 H. Colin-York, Y. Javanmardi, L. Barbieri, D. Li, K. Korobchevskaya, Y. Guo, C. Hall, A. Taylor, S. Khuon, G. K. Sheridan, T.-L. Chew, D. Li, E. Moeendarbary and M. Fritzsche, *Nano Lett.*, 2019, **19**, 4427–4434.
44 R. Heintzmann and T. Huser, *Chem. Rev.*, 2017, **117**, 13890–13908.

 This journal is © The Royal Society of Chemistry 2022